Synthesis of M-UiO-66 (M = Zr, Ce or Hf) employing 2,5-pyridinedicarboxylic acid as a linker: defect chemistry, framework hydrophilisation and sorption properties

(Article begins on next page)

Formic acid-based synthesis of M-UiO-66 (M = Zr, Ce or Hf) employing on 2,5-pyridinedicarboxylic acid as linker: defect chemistry, framework hydrophilisation and sorption properties

S. Waitschat, D. Fröhlich, H. Reinsch, H. Terraschke, K. A. Lomachenko, C. Lamberti, D. Broich, H. Kummer, T. Helling, M. Baumgartner, S. Henninger and N. Stock

Formic acid-based synthesis of M-UiO-66 (M = Zr, Ce or Hf) employing on 2,5-pyridinedicarboxylic acid as linker: defect chemistry, framework hydrophilisation and sorption properties

S. Waitschat[a], D. Fröhlich[b], H. Reinsch[a], H. Terraschke[a], K. A. Lomachenko[c,d], C. Lamberti[d,e], D. Broich[a], H. Kummer[b], T. Helling[b], M. Baumgartner[b], S. Henninger[b] and N. Stock[a]

[a] Institut für Anorganische Chemie, Christian-Albrechts-Universität, Max-Eyth-Straße 2, D 24118 Kiel, Germany. E-mail: stock@ac.uni-kiel.de
[b] Fraunhofer-Institute for Solar Energy Systems ISE, Heidenhofstrasse 2, 79110 Freiburg, Germany
[c] European Synchrotron Radiation Facility, 71 Avenue des Martyrs, CS 40220, 38043 Grenoble Cedex 9, France
[d] IRC "Smart Materials", Southern Federal University, Zorge str. 5, 344090 Rostov-on-Don, Russia
[e] Department of Chemistry, CrisDi Centre and INSTM Reference Center, University of Turin, Via Giuria 7, 10125 Turin, Italy

Abstract

Metal-organic organic frameworks of general composition $[M_6(OH)_4(O)_4(PDC)_{6-x}(Cl)_{2x}(H_2O)_{2x}]$ with M = Zr, Ce, Hf, PDC^{2-} = 2,5-pyridinedicarboxylate and $0 \leq x \leq 2$ were obtained under reflux using acetic acid as the solvent. Rietveld-refinements were carried out and confirmed that the MOFs crystallise in the UiO-66 type structure with different defect concentrations. Further characterization was carried out by NMR-spectroscopy, thermogravimetric analysis, Zr K-edge EXAFS and Ce L_3 XANES measurements. To highlight the influence of the additional nitrogen atom of the pyridine ring, luminescence and vapour sorption measurements were carried out. The hydrophilisation of the MOFs was shown by the adsorption of water at lower p/p_0 (< 0.2) values compared to the corresponding BDC-MOFs (0.3). For the water and methanol stability cycling vapour adsorption experiments were carried out to evaluate the MOFs as potential adsorbents in heat transformation applications.

1. Introduction

The increasing demand for heating and cooling in the worldnecessitates the development of new materials and technologies.[1,2] The use of low temperature waste energy in adsorptive heat transformation applications is one promising technology to improve energy efficiency.[3] Water as a working fluid of choice has numerous advantages, not the least in reducing the amount of world-wide used chlorofluorocarbons (CFCs) by the year 2047 as decided in the Montreal protocol of the UN.[4] Thus, adsorptive cooling and heating could replace conventional heat pumps or air conditioning systems, which employ CFCs. As another advantage, lowering of CO_2 emission is feasible since low temperature waste energy is employed in this process.[5] The industrially most relevant method for adsorptive heat transformation is a two-cycle process. Water is preferably employed due to its high enthalpy of evaporation (2500 kJ kg^{-1}), abundance and non-toxicity.[5] Furthermore, methanol and ethanol are good candidates as working fluids, especially when the sorption material is not water stable or when low temperatures must be achieved.[6] In the working cycle the dry adsorbent adsorbs a working fluid and the heat of adsorption is released to the environment ($Q_{ads.}$).[5] When the sorption material is saturated with a working fluid, the second cycle,

the regeneration cycle, starts. To desorb the working fluid, energy is necessary, which ideally would be waste heat from a different process ($Q_{des.}$). Thus, in this step, energy is consumed from the environment and cold is produced. Due to the condensation of the working fluid in a spatially separated reservoir, heat is produced again ($Q_{con.}$).[3] Hence the machine can work as an adsorption heat pump when intermediate temperatures (Q_{ads} and $Q_{con.}$) are used, or as a adsorption chiller when a lower temperature of Qevap. is used.[3]

For a good performance, the sorption material should have several properties. It must be stable during thousands of ad-/ desorption cycles and should exhibit a high uptake (sorption capacity). Additionally, the isotherm should exhibit no hysteresis and have a sigmoidal shape in a p/p_0-range from 0.05 to 0.3.[7] While different adsorbents like silica gel, zeolites or SAPOs have already been employed in commercial cooling systems compounds known as MOFs (metal–organic frameworks) have recently emerged as alternative adsorbents showing superior performance.[3,8,9]

MOFs are composed of inorganic building units, usually metal ions or metal-oxygen clusters, which are interconnected by organic linker molecules.[10] They exhibit a remarkable structural diversity due to their modular composition.[11,12] The adsorbent with the highest water capacity is Cr-MIL-101 ($[Cr_3F(H_2O)_2O(1,4-BDC)_3]$, $1,4-BDC^{2-}$ = 1,4-benzenedicarboxylate, MIL = Material Institute Lavoisier), however, the uptake is in the range $0.3 \leq p/p_0 \leq 0.6$.[13,14] Several thousand cycles of water vapour ad-/desorption without any loss of capacity was demonstrated for MIL-53-Fum ($[Al(OH)(Fum)]$, Fum^{2-} = fumarate)[15] and CAU-10 ($[Al(OH)(1,3-BDC)]$, $1,3-BDC^{2-}$ = 1,3-benzenedicarboxylate, CAU = Christian-Albrechts-Universität)[16,17]These compounds exhibit high capacities and sigmoidal isotherms below $p/p_0 < 0.3$.[17]
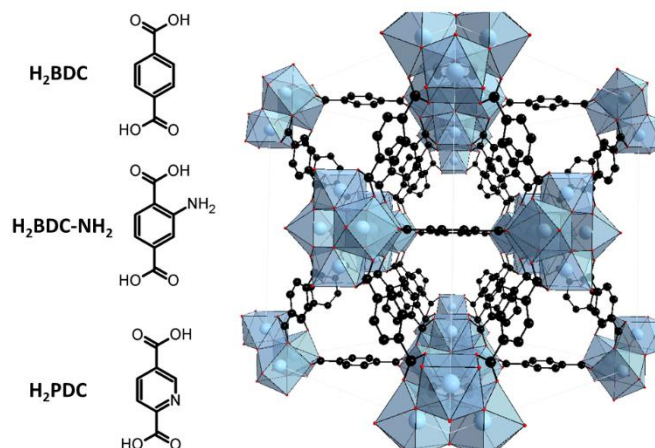

Fig. 1 Three linker molecules (left) that have been used for the synthesis of UiO-66 (right).

There exist several ways to fully exploit the modular structure of MOFs in order to tailor the water sorption behaviour. In particular, the influence of hydrophilic groups on the sorption properties was investigated. Thus, formally replacing a –CH– group in 2-methylimidazole (HMIM) by –N– leads to the formation of a linker HMTZ (3-methyl-1,2,4-triazole). The resulting compounds $[Zn(MIM)_2]$ and $[Zn(MTZ)_2]$ exhibit very different water sorption properties. While the first compound is not porous, the latter is porous towards water.[18] A similar approach has been reported for the modification of CAU-10. 1,3-Benzenedicarboxylic acid was replaced by 3,5-pyridinedicarboxylic acid or 2,5-furandicarboxylic acid as linker molecules. The incorporation of more hydrophilic linker molecules leads to a higher uptake of water and a shift to lower p/p_0 values compared to the parent compound.[19] In addition, the influence of additional amine groups was investigated for UiO-66 ($[Zr_6(O)_4(OH)_4(BDC-NH_2)_6]$, UiO = University of Oslo).[20–22] UiO-66-NH$_2$ not only shows a shift of the water uptake to lower p/p_0 ranges but also a lower total uptake due to the steric demand of the NH$_2$-group (Fig. 1).

Based on these results one could anticipate that the incorporation of N-heterocyclic linker molecules into the UiO-66 structure could lead to an increase in the sorption capacity and a shift to

3

lower relative humidity values. Very recently the partial incorporation of 2,5-pyridinedicarboxylate (PDC^{2-}) by solventassisted- linker-exchange (SALE) has been reported,[23] while the synthesis in DMF[24] or in a water/acetic acid mixture[25] leads to Zr-UiO-66-PDC, although no structure determination and water sorption behaviour were carried out in these studies.

Here, we describe the synthesis and detailed characterization of three UiO-66-type compounds containing Zr, Ce or Hf in the IBU and 2,5-pyridinedicarboxylate instead of 1,4-benzenedicarboxylate ions, i.e. Zr-, Ce- and Hf-UiO-66-PDC. In addition, water and methanol sorption properties are reported.

2. Experimental
2.1. Materials and methods
All chemicals were used as received. High throughput powder X-ray diffraction (PXRD) investigations were carried out using a Stoe Stadi P X-ray diffractometer equipped with a xy-stage in transmission geometry (MoK$_{\alpha 1}$ radiation, Mythen detector). PXRD patterns for structure determination were recorded with a Stoe Stadi P X-ray diffractometer in transmission geometry using CuK $_{\alpha 1}$ radiation and data were collected by a Mythen detector. Infrared (IR) spectra were recorded on a Bruker ALPHA-P A220/D-01 Fourier transform infrared (FTIR) spectrometer equipped with an attenuated total reflection (ATR) unit. NMR spectroscopy was carried out using a Bruker DRX 500 spectrometer. Thermogravimetric (TG) analysis was performed using a NETZSCH STA 429 CD analyser with a heating rate of 4 K min^{-1} under flowing air (flow rate: 75 ml min^{-1}). Elemental analysis was performed using a EuroVector Euro EA elemental analyser. Nitrogen and CO_2 sorption isotherms were measured at −196 °C and 25 °C, respectively, using a BELSORP-Max apparatus. MeOH sorption isotherms were obtained with a Quantachrome Autosorb and H_2O adsorption was measured with a Quantachrome Hydrosorb at 25 °C. Water cycling stabilities were examined on a Setaram™ TGA-DSC-111 on powdered samples. A humidified argon gas flow (40 °C, 76.3% relative humidity) was generated by using a Setaram WetSys humidity controller and passed through the sample chamber, while the temperature of the sample was varied and the mass of the adsorbent was monitored. For the multi-cycle ad-/desorption experiments, the temperature of the sample was varied between 40 °C and 140 °C with a cycle time of 5 h. Methanol cycling stability was examined using a Surface Measurement Systems Ltd DVS Vacuum. Before and after cycling, the sample was degassed at 90 °C in a vacuum and equilibrium points were taken at 25 °C by increasing the pressure of the gas flow at 5 ml min^{-1} and held constant at 115 hPa while varying the temperature of the sample between 25 and 100 °C, which corresponds to a rela- tive pressure p/p_0 of 0.671 and 0.033, with cycle times of 1 h

while cooling and 1 h on heating. In situ diffuse reflectance infrared Fourier transform spectroscopy (DRIFTS) measurement on Zr-UiO-66-PDC was carried out with a PerkinElmer Frontier spectrometer, equipped with a Diffuse Reflectance Accessory. A heat chamber with a ZnSe window was utilized for the in situ experiments. The spectra are averaged from 20 scans and recorded between 4000 and 700 cm^{-1} with a resolution of 4 cm^{-1}. Prior to the measurement the MOF was outgassed at 120 °C and reduced pressure. The experiment was conducted at 25 °C under a N_2 gas atmosphere with a flow rate of 100 ml min^{-1} controlled by using a Bronkhorst MassView. To investigate the influence of MeOH on the structure of the MOF, it was subjected 5 times to a MeOH dosed N_2 stream for 30 seconds. The N_2 stream was passed through a MeOH bath (298 K) with a bubble diffusor. After each treatment, the sample was treated with dry N_2 until equilibrium and the spectrum was recorded. Luminescence measurements of the solid samples were carried out in Suprasil A quartz ampoules at room temperature. For this purpose, a FL-22 Fluorolog3 spectrometer (Horiba Jobin Yvon GmbH), equipped with a 450 W xenon lamp, a R928P photomultiplier and an iHR-320-FA triple grating imaging spectrograph was applied. Reflection spectra were also recorded at room temperature from the powdered samples with a Cary 5000 spectrometer (Varian Techtron Pty.) applying $BaSO_4$ as a reference and diluting material. A Ce L$_3$-edge X-ray absorption near edge structure (XANES) spectrum of Ce-UiO-66-PDC was collected at

the Southern Federal University (Russia) using a Rigaku R-XAS spectrometer. An experimental Zr K-edge (17 998 eV) extended X-ray absorption fine structure (EXAFS) spectrum of Zr-UiO-66-PDC was collected at BM23 beamline[26] of the European Synchrotron Radiation Facility (ESRF). All the XAS measurements were conducted in transmission mode at room temperature. Experimental details of XAS data collection are provided in the ESI.† The ring was operated in a 16-bunch regime with a maximum current of 90 mA. Experiments were conducted in transmission mode using Ar/He-filled ionization chambers as detectors. Gas pressure in the chambers was 0.4 bar Ar, +1.6 bar He for I_0 and 2 bar of Ar for I_1 resulting in roughly 20% and 70% absorption respectively. A Si (111) double-crystal monochromator was used for energy scanning, while Rh-coated mirrors positioned at an incidence angle of 3 mrad were employed for harmonic rejection. The sample was prepared in the form of self-supporting pellets (80 mg of powder in a 13 mm diameter disk, pressed with a force <500 kgf) resulting in the edge jump of 1.5. Measurements were conducted at room temperature. Excellent performance of the beamline allowed the data collection up to $k = 23$ Å^{-1} with a high signal-to-noise ratio.

2.2. Synthesis

The high-throughput investigations for the synthesis of the new compounds were carried out in a steel multiclave equipped with 24 Teflon reactors with a volume of 2 ml each.[27] Different metal salts, solvent combinations as well as modulators were tested. The optimization of reaction time and temperature was performed in Pyrex glass tubes with a volume of 5 ml, which were heated and stirred in an aluminium block by using a laboratory heating plate. Details of the synthesis optimisation are listed in the ESI (SI2, SI3, and SI4†). The optimized reaction conditions for the scale-up to 50 ml reactors under reflux are described below.

2.2.1. Synthesis of Zr-UiO-66-PDC. 0.733 g (4.4 mmol) H$_2$PDC and 1.434 g (4.4 mmol) ZrOCl$_2$·8H$_2$O were mixed in 45 ml formic acid and 5 ml water in a round bottom flask placed in an oil bath. The mixture was heated at 120 °C under reflux for 3 h. The reaction was quenched by placing the round bottom flask under cold water. The suspension was separated by centrifugation and subsequently washed twice with water and one time with ethanol (6000 rpm, 30 min, each). The product was dried under ambient conditions (yield: 1.56 g).

2.2.2. Synthesis of Ce-UiO-66-PDC. 1.670 g (10 mmol) H$_2$PDC and 5.480 g (10 mmol) (NH$_4$)$_2$[Ce(NO$_3$)$_6$] were mixed in 5 ml conc. HNO$_3$ and 45 ml water in a round bottom flask. The mixture was heated at 90 °C under reflux for 30 minutes. The reaction was quenched by placing the round bottom flask under cold water. The suspension was separated by centrifugation and subsequently washed twice with water and one time with ethanol (6000 rpm, 30 min, each). The product was dried under ambient conditions (yield: 3.25 g).

2.2.3. Synthesis of Hf-UiO-66-PDC. 0.835 g (5 mmol) H$_2$PDC and 1.6 g (5 mmol) HfCl$_4$ were mixed in 25 ml acetic acid and 25 ml water in a round bottom flask. The mixture was heated at 120 °C under reflux for 3 h. The reaction was quenched by placing the round bottom flask under cold water. The suspension was separated by centrifugation and subsequently washed twice with water and one time with ethanol (6000 rpm, 30 min, each). The product was dried under ambient conditions (yield: 1.48 g).

3. Results and discussion

Using high-throughput methods, we have been able to establish the water-based synthesis of three UiO-66-PDC compounds containing Zr^{4+}, Ce^{4+} or Hf^{4+} ions on a g-scale using reflux conditions. Products of high crystallinity were obtained using different modulators.

3.1. Crystallography and defect chemistry

The structures of the three compounds M-UiO-66-PDC (M = Zr, Ce, and Hf) were refined from PXRD data (Fig. 2) using the Rietveld method by fixing the occupancy of the linker according to the results of the TG measurements (section S5.1, Table S5.1 and Fig. S5.1, S5.4, S5.7†).[28] In order to further confirm the presence of defects in the zirconium and hafnium based MOFs, the Rietveld refinement was also carried out by fixing the occupancy of the linker molecules to 1, hence assuming an ideal framework composition. While the Rietveld plots hardly change, the figures of merit are evidently inferior to the values obtained by refinement of the defective frameworks (Table S5.2†). Hence our results show that our structural models describe the data well. All three structures are related to the ideal UiO-66 type framework and contain the hexanuclear clusters $[M_6(O_4)(OH)_4]^{12-}$ with M = Zr^{4+}, Ce^{4+} and Hf^{4+} respectively. In the ideal structure each cluster is connected by twelve terephthalate ions,[29] however compounds with linker and cluster defects are known.[30–33]
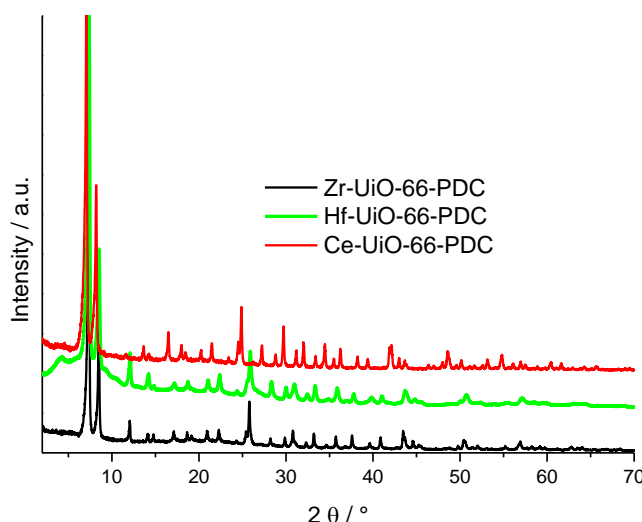

Fig. 2: PXRD patterns of the M-UiO-66-PDC compounds (M = Zr^{4+} Ce^{4+} and Hf^{4+}).

According to the results of the TG measurements, all three MOFs show different types of defect chemistry. The PXRD patterns of Zr- and Ce-UiO-66-PDC exhibit exclusively peaks that are consistent with the **fcu** topology (Fig. 2). The Rietveld refinements of the PXRD data support the absence of linker defects in the Ce-MOF. Thus, the compound has the ideal composition $[Ce_6(O)_4(OH)_4(PDC)_6]$. The oxidation state of cerium in the compound was verified by XANES measurements, which confirmed that only Ce^{4+} is present in Ce-UiO-66-PDC (Fig. S5.11†). In contrast, the structure of the Zr-MOF was successfully refined with one statistically missing linker molecule per formula unit by fixing the site occupancy of the linker during the calculations. The composition of the product and the presence of Cl^- ions for charge balance were confirmed by TG analysis (Fig. S9.4†), NMR spectroscopy (Fig. S6.1†) and EDX measurements (ratio Zr : Cl = 3 : 1). Although the localisation of H atoms is not possible and O, OH and H_2O cannot be distinguished, the analytical data confirm the formula of Zr-UiO-66-PDC as $[Zr_6(O)_4(OH)_4(Cl)_2(H_2O)_4(PDC)_5]$.

To complement the results of the PXRD data, Zr K-edge EXAFS analysis of Zr-UiO-66-PDC was performed using a Zr-UiO-66-PDC sample washed with ethanol (for details see Fig. S5.10†). A fitting model included the nearest shells of one of the six equivalent Zr atoms in a UiO-66 cornerstone (Fig. 3a). Compared to the classical model proposed by Valenzano et al.,[34] several modifications were made based on the input of complementary techniques. First, the presence of missing linker defects was modelled by setting the degeneracy of the Zr–C path to 3.3 instead of 4, mimicking the C-site occupancy of 0.83 as supported by PXRD and TG measurements. Then, since a Cl-containing salt was used in the synthesis and chloride was detected in the material by EDX

analysis, the presence of the chloride ion at the position of missing linkers was assumed, following the thorough study of Shearer et al.[35] Accordingly, the degeneracy of the introduced Zr–Cl path was set to $4 - 3.3 = 0.7$. With reference to the O-coordination, two μ_3-OH oxygens were parameterized together with the four carboxyl oxygen atoms (O1) in the same way as reported in the work of Valenzano et al.[34] due to the similarity of the lengths of these scattering paths.[36] Conversely, two μ_3-O atoms were parameterized as a separate shell. Then, two zirconium shells were considered: four Zr neighbors in the plane of the octahedron (Zr1) and one Zr atom at the opposite vertex (Zr2). In contrast to all the abovementioned single-scattering shells, the Debye–Waller factor and bond elongation parameter for the Zr–Zr2 path were not independent, but derived from the corresponding parameters of the Zr–Zr1 path in order to decrease the number of free parameters in the fit using the assumption that the octahedron may only be isotropically distorted.
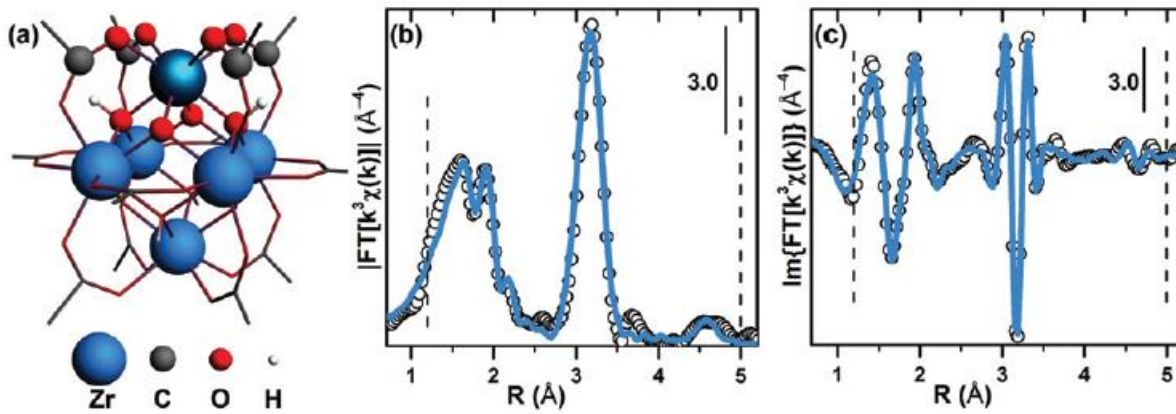

Fig. 3 (a) Structural model of the UiO-66 cornerstone. Absorbing Zr atom is highlighted, atoms included in the EXAFS fitting model (except for H) are shown as spheres. (b) Modulus and (c) imaginary part of the experimental (scattered circles) k^3-weighted phase-uncorrected Zr K-edge EXAFS FT for Zr-UiO-66-PDC together with the fit (blue line) made using the mode from panel a. Fitting range (1.2–5.0 Å) is shown by the vertical dotted lines.

Table 1 Fit details and best-fit parameters for Zr K-edge EXAFS of Zr- UiO-66-PDC, presented in Fig. 3. Coordination numbers (left column) and atomic distances (right column) are given in parentheses

	Zr-UiO-66-PDC
R-Factor	0.017
Fitting range in k, Å^{-1}	3.7–20.6
Fitting range in R, Å	1.2–5.0
Number of independent points	40
Number of fitting parameters	12
S_0^2	1.00 ± 0.06
ΔE, eV	-1.3 ± 0.8
$R_{\mu_3\text{-O}}$, Å ($N = 2$)	2.07 ± 0.005 (2.13)
$\sigma_{\mu_3\text{-O}}^2$, Å^2	0.003 ± 0.0004
R_{O1}, Å ($N = 6$)	2.22 ± 0.005 (2.26)
σ_{O1}^2, Å^2	0.006 ± 0.0005
R_{Cl}, Å ($N = 0.7^a$)	2.49 ± 0.01
σ_{Cl}^2, Å^2	0.006 ± 0.001
R_C, Å ($N = 3.3^a$)	3.17 ± 0.02 (3.13)
σ_C^2, Å^2	0.006 ± 0.002
R_{Zr1}, Å ($N = 4$)	3.52 ± 0.003 (3.50)
σ_{Zr1}^2, Å^2	0.005 ± 0.0002
R_{Zr2}, Å ($N = 1$)	4.98^b (4.94)
σ_{Zr2}^2, Å^2	0.006^b
|Highest correlations|	$\Delta R_{Zr1}/\Delta E = 0.87$
	$\sigma_{Zr1}^2/S_0^2 = 0.86$
	|Others| <0.8

^{a} NC and NCl were set to 3.3 and 0.7 respectively to simulate the missing linker defects detected by PXRD, TG, NMR, and EDX measurements. ^{b} R_{Zr2} and σ_{Zr2}^2 were derived from the values of R_{Zr1} and σ_{Zr1}^2 respectively.

Overall, the fit demonstrated good agreement with the experimental data yielding physically meaningful parameters (Fig. 3b, c and Table 1). Interestingly, although the splitting of the first EXAFS maximum indeed appears due to the presence of the two distinct oxygen shells (4 O1 + 2 μ_3-OH and 2 μ_3-O), the two peaks cannot be attributed to each of them separately. Conversely, such splitting in the modulus of the Fourier-transformed (FT) EXAFS data is justified by the partial cancellation of the signals from these two shells in the 1.75–1.8 Å range (phase-uncorrected) due to the significantly different bond lengths (2.07 Å for μ_3-O vs. 2.22 Å for O1).

The PXRD pattern of Hf-UiO-66-PDC shows a broad peak at low 2 theta values compared to the **fcu** structure of the parent framework (Fig. 2). These peaks are due to the correlated nanoscale disorder in the crystal structure and are well known for Hf-UiO-66-BDC.[37,38] In these regions missing linkers and missing clusters result in a structure with the reo topology. Detailed characterisation by TG analysis (Fig. S9.6†), NMR spectroscopy (ESI Fig. S6.3†) and EDX analysis (ratio Hf : Cl = 3 : 2) excludes the presence of acetate ions and demonstrates the presence of Cl^- ions. The deduced formula is $[Hf_6(O)_4(OH)_4(Cl)_4(H_2O)_8(PDC)_4]$ and a Rietveld refinement, neglecting the additional peaks originating from the **reo** defect topology, and fixing the occupancy of the linker to the value obtained from the TG measurement supports the composition. The structural model obtained indicates that statistically missing linker defects in the **fcu** framework of Hf-UiO-66-PDC lead to an identical composition as also present in the defect **reo** domains.

3.2. Thermal and chemical stabilities

Thermogravimetric analyses and temperature dependent PXRD experiments were carried out for all three MOFs to verify the deduced formulas and monitor the thermal stability. According to the PXRD data Zr-UiO-66-PDC is stable up to a temperature of 220 °C (Fig. S9.1†). The first weight loss up to 260 °C in the TG curve could be explained by the dehydration and loss of the HCl. Framework decomposition starts at approximately 300 °C (Fig. S9.4†). These observations indicate that the structure collapses at lower temperatures while thermal combustion is delayed up to higher temperatures. The weight loss corresponds to five linker molecules per cluster. Thus, the postulated sum formula of Zr-UiO-66-PDC is confirmed as $[Zr_6(O)_4(OH)_4(Cl)_2(H_2O)_4(PDC)_5]$. A similar behaviour of the thermal stability is observed for Ce- and Hf-UiO-66-PDC. Ce-UiO-66-PDC is stable up to 150 °C but combustion starts at 250 °C (Fig. S9.2 & S9.5†). The TG analysis indicates an ideal composition of six linker molecules per cluster. Thus, the deduced formula for Ce-UiO-66-PDC is confirmed as $[Ce_6(O)_4(OH)_4(PDC)_6]$. Hf-UiO-66-PDC is stable up to 150 °C based on the PXRD data (Fig. S9.3†) but combustion is delayed up to 200 °C (Fig. S9.6†). The TG analysis proves the presence of defects in the structure and is in agreement with four linker molecules and four chloride ions per cluster. Thus, the postulated sum formula of Hf-UiO-66- PDC is confirmed as $[Hf_6(O)_4(OH)_4(Cl)_4(H_2O)_8(PDC)_4]$.

The chemical stability of the title compounds was studied by stirring 20 mg of each sample in 1 ml different organic solvents and different concentrations of aqueous HCl and NaOH for 24 hours at room temperature. All three MOFs are stable in a pH-range from 1 to 12 and in more basic solutions the MOFs are destroyed. None of the MOFs is stable in a 0.1 M phosphate buffer (Na_2HPO_4/NaH_2PO_4). All three MOFs are stable in the tested organic solvents (Fig. S9.7–S9.12†).

3.3. Luminescence properties

To study the influence of the N-atom in the aromatic ring on the luminescence properties, the emission spectra of the title compounds and linker molecules H_2PDC and H_2BDC were recorded applying the excitation energies listed in Table 2 (Fig. 4, Fig. S10.1–S10.5†). Since radiative electronic transitions in the UV-Vis region are not possible in Zr^{4+} and Hf^{4+}, the optical properties of these MOFs are caused exclusively by the aromatic units of the organic linker, as often reported for other transition metal MOFs.[39–41] The emission spectrum of Zr-UiO-66-PDC (Fig. 4, blue curve) consists of a broad band in the UV-blue spectral range with full width at half maximum (FWHM) of 3836 cm^{-1} and maximum at 24752 cm^{-1} (Table 2 and Fig. S10.1†). This band is blue-shifted in

comparison with the emission spectrum of the H$_2$PDC linker, which has an emission maximum located in the green spectral range at 19197 cm^{-1} with a similar FWHM of 3828 cm^{-1} (Fig. 4, red curve). Similar values were reported by Sun et al. for other MOFs containing PDC^{2-} ions.[42] The blue shift after the incorporation of the organic linker into the MOF structure is explained in the literature by the enhancement of the $\pi \rightarrow \pi *$ energy due to the weakening effect of the skeleton vibration within the rigid framework.[43] This shift to higher energy is also observed in the emission spectrum of Hf-UiO-66-PDC (Fig. 4, black curve), broadly distributed between approximately 15000 cm^{-1} and 26 000 cm^{-1} with a maximum at 20903 cm^{-1}. In addition, the luminescence spectrum of Hf-UiO-66-PDC shows a second emission band of lower intensity with a maximum at 24420 cm^{-1}. As observed in the recorded excitation spectra (Fig. S10.3†), the energy assigned to this band is self-absorbed by Hf-UiO-66-PDC, decaying radiatively through the emission at ca. 20000 cm^{-1}. In contrast, Ce-UiO-66-PDC is not luminescent. Most probably, the blue shift of the emission band in comparison with H$_2$PDC causes the overlap between the linker-based emission band and the absorbed spectral region of the Ce-UiO-66-PDC, shown by the diffuse reflectance spectra in Fig. S10.7† as previously observed for Ce-CAU-24.[41]

Table 2 Emission maximum, excitation energy and FWHM of emission spectra of H$_2$PDC, Hf-UiO-66-PDC, Zr-UiO-66-PDC, H$_2$BDC, Zr-UiO-66-BDC and Hf-UiO-66-BDC

Compound	Emission maximum	Excitation energy	FWHM
H$_2$PDC	19 197 cm^{-1}	27 777 cm^{-1}	3828 cm^{-1}
Hf-UiO-66-PDC	20 903 cm^{-1}	27 777 cm^{-1}	6885 cm^{-1}
Zr-UiO-66-PDC	24 752 cm^{-1}	27 777 cm^{-1}	3836 cm^{-1}
H$_2$BDC	25 900 cm^{-1}	30 769 cm^{-1}	4357 cm^{-1}
Zr-UiO-66-BDC	26 532 cm^{-1}	30 769 cm^{-1}	4498 cm^{-1}
Hf-UiO-66-BDC	26 022 cm^{-1}	30 769 cm^{-1}	4704 cm^{-1}

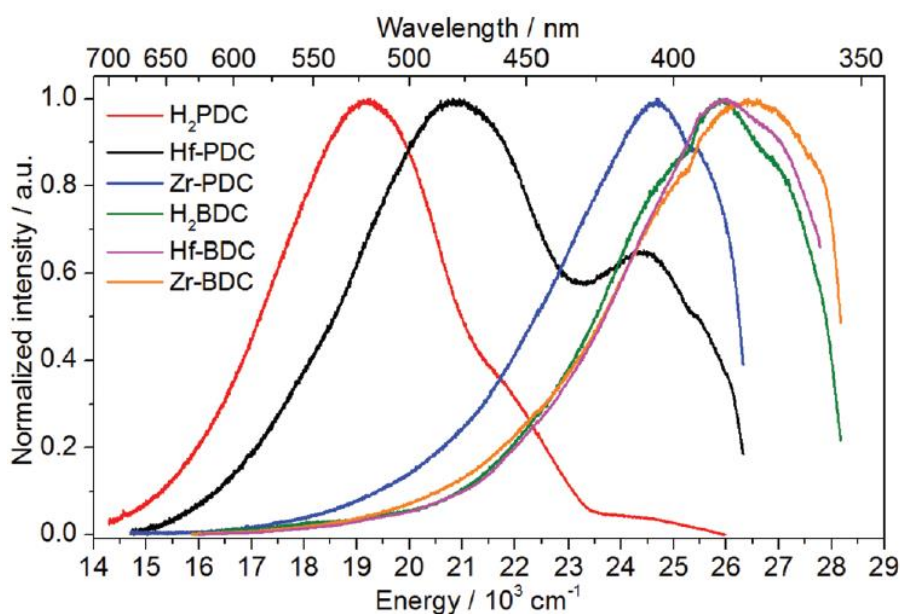
Fig. 4 Emission spectra of H2PDC (red curve), Hf-UiO-66-PDC (blackcurve) and Zr-UiO-66-PDC (blue curve) as well as H2BDC (green curve),Hf-UiO-BDC (pink curve) and Zr-UiO-66-BDC (orange curve), applying excitation energies listed in Table 2.

The emission spectrum of Zr-UiO-66-BDC (Fig. 4, orange curve) is located mostly in the UV spectral range with a maximum at 26532 cm^{-1} (FWHM = 4498 cm^{-1}). In comparison with the H$_2$BDC linker (Fig. 4, green curve) it is also blueshifted. The same shift in emission maxima was

reported for Zn terephthalates.[43] Similarly for the MOFs containing the H2PDC linker, the emission band measured for Hf-UiO-66-BDC (Fig. 4, pink curve) is also slightly blue-shifted in comparison with the emission band of the H2BDC linker, with a maximum at 26022 cm^{-1} and FWHM of 4704 cm^{-1}. The red shift between the emission spectra of PDC^{2-} and BDC^{2-} based structures has been previously observed for Zn-containing coordination polymers[42] and similar shifts between Zr-UiO-66 and Hf-UiO-66 as well as shifts caused by the functionalization of the H2BDC ligand with NH_2 groups have been reported by Yasin et al.[44] However, the cause for these effects still remains an open question and additional experiments are necessary for explaining these phenomena. In general, according to Yang et al. the additional lone pairs of the nitrogen atoms are advantageous for interacting with the π^* orbitals of the aromatic ring, enhancing the luminescence efficiency of the analogue H2PDC linker.[45] Moreover, the incorporation of N-heterocyclic linker molecules in MOFs has been reported to lead to an increase in the host–guest interactions with various guest species as well as enhanced luminescence properties, enabling the application of the modified UiO-66 compounds as sensor materials in the detection of Fe^{3+},[46] [phosphates][45] and biological thiols.[47]

3.4. Gas sorption

To investigate the influence of the N-atom in the aromatic ring on the sorption properties, N_2, CO_2, H_2O and MeOH isotherms were recorded at -196 and 25 °C for N_2 and the other gases, respectively. Although Zr-and Ce-UiO-66-PDC were successfully activated at 120 °C for 16 hours under reduced pressure, the removal of guest molecules in Hf-UiO-66-PDC, even at ambient temperature and a pressure of 0.1 mbar, led to the destruction of the structure (Fig. S11.2†). Zr- and Ce-UiO-66-PDC showed type I isotherms (Fig. 5) and evaluation by the BET method resulted in specific surface areas of S_{BET} = 1380 and 768 m^2 g^{-1}, respectively. The difference is due to the different number of linker defects and the higher molar masses of the Ce-MOF. Compared to the known Zr- and Ce-UiO-66-BDC structures, the uptake of the corresponding PDC-MOFs is higher for the Zr-MOF (lit.: S_{BET} = 1105 m^2 g^{-1})[35] but lower for the Ce-MOF (lit.: S_{BET} = 1282 m^2 g^{-1}).[31] These observations also confirm the linker defects observed in Zr-UiO-PDC and Ce-UiO-66-BDC. Both MOFs are also porous towards $CO2$ (Fig. 5 and Table S11.1†).

The volumetric H_2O and MeOH sorption isotherms of Zr-UiO-66-PDC and Ce-UiO-66-PDC show a type 1b shape (Fig. S11.4 and Fig. S11.5†). Due to the very strong hydrophilic adsorbent–adsorbate interactions uptake at $p/p_0 < 0.01$ takes place. For water as the adsorptive, a linear uptake at $p/p_0 > 0.3$ is observed. At this point (p/p_0 = 0.2) Zr-UiO-66-PDC adsorbs 0.34 g g^{-1} and Ce-UiO-66-PDC 0.23 g g^{-1} water. In comparison with Zr-UiO-66-BDC and –BDC-NH_2 a shift of the main uptake from p/p_0 = 0.3 in Zr-UiO-66-BDC to <0.2 in Zr-UiO-66-PDC is observed, while the absolute amount of H_2O vapour adsorbed is very similar (0.34 g g^{-1} and 0.35 g g^{-1} for Zr-UiO-66-PDC and Zr-UiO-66-BDC respectively, Fig. 6).[18] Although small changes of the sorption properties could be due to different degrees of dehydroxylation of the hexanuclear Zr–O clusters, we anticipate that these shifts are much better explained by the hydrophilicity of the different linker molecules in the UiO-66-type structures.

The affinity at low p/p_0 values of the materials towards MeOH is comparable to the affinity towards water. The total capacity for both MOFs is similar with 0.31 and 0.30 g g^{-1} for Zr- and Ce-UiO-66-PDC, respectively, which are relatively high numbers, compared to the values reported in the literature (Table S11.2†).[3]

Due to the water uptake of 0.34 g $g-1$ in the region $0.01 < p/p_0 < 0.3$, the water stability of M-UiO-66-PDC (M = Zr and Ce) was tested by a multicycle ad-/desorption experiment in a thermogravimetric balance (Fig. 7). In this experiment a humidified argon gas flow of constant relative humidity is passed through the sample chamber and the temperature of the sample is varied (40 and 140 °C) and the mass of the adsorbent is monitored. Under cycling conditions, Zr-UiO-66-PDC shows a very small dry mass degradation from 19.22 mg to 18.94 mg (2.5 wt%). During the cycle treatment a strong decrease in uptake capacity takes place after the first adsorption step, of

about 30%, which remains relatively constant for the following adsorption steps. During the 20 ad-/desorption cycles a decrease in the water uptake capacity $((m_{ads-H2O} - m_0)/m_0)$ from 0.39 to 0.26 g g^{-1} is observed (Fig. 7), which levels out to a constant value of 0.25 g g^{-1} after an additional 20 cycles. This degradation is probably due to a structural change after the first ad-/desorption, which lowers the adsorption capacity, as the dry mass remains nearly constant but the uptake decrease is already stabilised after this first cycle. Compared to Zr-UiO-66-PDC and –BDC-NH$_2$ which show a substantial and continuous loss of water capacity in the cycling experiments, the Zr-UiO-66-BDC shows a higher stability.[20] Ce-UiO-66-PDC shows a similar behaviour in the cycling experiments but due to its lower thermal stability the degradation is faster (Fig. S12.1†).
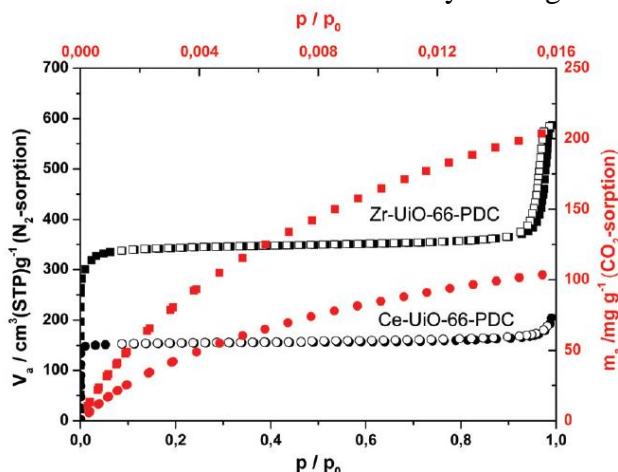

Fig. 5 Nitrogen (black curves, left and bottom axes) and CO$_2$ (red curves, right and top axes) isotherms of Zr-UiO-66-PDC (squares) and Ce-UiO-66-PDC (circles) measured at −196 °C and 25 °C respectively. For the nitrogen isotherms, full and open symbols refer to adsorption and desorption respectively.
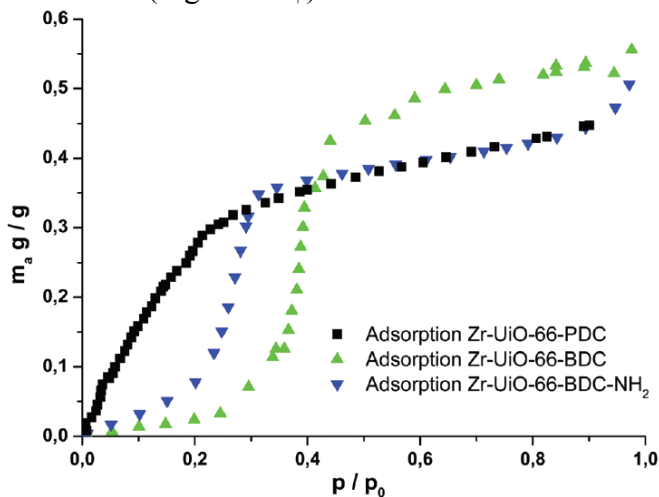

Fig. 6 Comparison of the H$_2$O isotherms of Zr-UiO-66-PDC (black), Zr-UiO-66-BDC-NH$_2$ (blue)[20] and Zr-UiO-66-BDC (green)[20] measured 25 °C.

Additionally the methanol ad-/desorption cycling stability of Zr-UiO-66-PDC was examined in an in situ experiment using a Surface Measurement Systems Ltd DVS Vacuum in a temperature range between 25 and 100 °C. Parameters were chosen to mimic an adsorption chiller for cooling applications around 10 °C. The material treated for 100 cycles exhibited an increase in dry mass from 25.86 mg to 26.12 mg due to the exchange of the hydroxyl groups by methoxy groups (Fig. S13.1†). After a fast decline in the methanol uptake during the first cycles the decrease in capacity shows a small but continuous behaviour (Fig. 8). The total methanol capacity $((m_{ads-MeOH} - m_0)/m_0)$ of about 0.41 g g^{-1} drops constantly down to about 0.21 g g^{-1} after 100 cycles. A plateau could not be reached due to instrumental limits of the set-up. The strong decrease at the beginning can be explained by a post-synthetic exchange of the hydroxyl groups by methoxy groups, which has been reported previously[48] and is confirmed by diffuse reflectance infrared Fourier transform spectroscopy (DRIFTS) (Fig. S13.1†). Upon treatment with methanol new bands at 2928 and 2824 cm^{-1} evolve which are assigned to the C–H stretchings of the methoxy groups. The intensity of the band at 2742 cm^{-1}, assigned to the hydrogen-bonded OH/OH$_2$ groups in the hexanuclear cluster node, decreases simultaneously.[48] Zr-UiO-66-PDC exhibits a lower stability compared to other MOFs such as HKUST-1 or MIL-101(Cr)[49] under methanol ad-/desorption conditions.
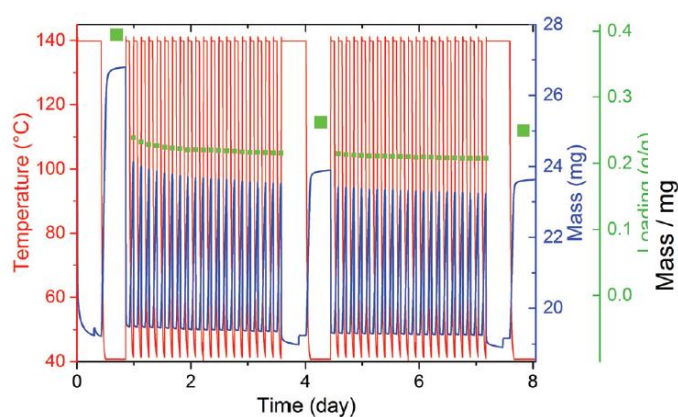
Fig. 7 Thermogravimetric water adsorption/desorption cycling experiments for 40 cycles of Zr-UiO-66-PDC. Long segments at the beginning and at the end of each experiment were conducted to determine the equilibrium loading of the sample (red: sample temperature, blue: mass, green: loading to the corresponding ad-/desorption pair). Adsorption temperature: 40 °C, desorption temperature: 140 °C, 76.3% RH at adsorption.
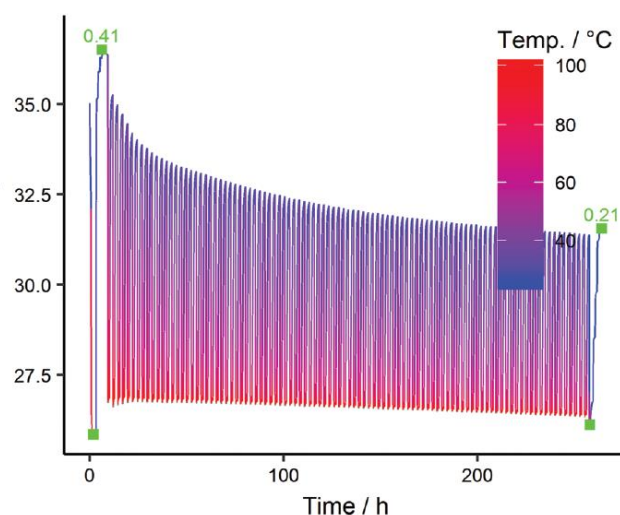

Fig. 8 Thermogravimetric methanol adsorption /desorption cycling experiments for 100 cycles of Zr-UiO-66-PDC (blue: mass). Adsorption from 25 °C (blue) to desorption 100 °C (red), 67.1% of the saturation pressure of MeOH at 25 °C. Green squares: loading of the first and last ad-/desorption pairs.

4. Conclusions

In conclusion, we synthesised three new MOFs with 2,5-pyridinedicarboxylic acid as a linker and Zr^{4+}, Hf^{4+} and Ce^{4+} respectively. All compounds could be fully characterized by combining the results of various characterization techniques, like TG analysis, NMR- and IR spectroscopy and Rietveld refinement using fixed occupancies of the linker molecules. The latter results show that the structural models describe the PXRD data well. The Zr- and Ce-MOFs are porous towards N_2, CO2, H_2O and MeOH. The influence of the additional nitrogen atom in the ring, compared to UiO-66-BDC was investigated by luminescence spectroscopy and sorption measurements. The water sorption measurements show similar capacity of water compared to UiO-66-BDC but a steeper adsorption at lower p/p_0 values. The possibility for the use in heat transformation application was tested with cyclic vapour sorption measurement with water and methanol. The water sorption measurements show that the stability of the MOFs is not perfect and the MeOH measurements show a decrease in the total uptake which correspond to an exchange of the OH– groups to the methoxy groups.

Conflicts of interest

There are no conflicts to declare

Acknowledgements

Notes and references

1 M. Isaac and D. P. van Vuuren, *Energy Policy*, 2009, **37**, 507–521.
2 M. Sivak, *Energy Policy*, 2009, **37**, 1382–1384.
3 M. F. de Lange, K. J. F. M. Verouden, T. J. H. Vlugt, J. Gascon and F. Kapteijn, Chem. Rev., 2015, **115**, 12205–12250.
4 U. N. E. P. O. Secretariat, Handbook for the Montreal protocol on substances that deplete the ozone layer, UNEP/Earthprint, 2006.

5 F. Jeremias, D. Fröhlich, C. Janiak and S. K. Henninger, *New J. Chem.*, 2014, **38**, 1846.

6 M. F. de Lange, B. L. van Velzen, C. P. Ottevanger, K. J. F. M. Verouden, L.-C. Lin, T. J. H. Vlugt, J. Gascon and F. Kapteijn, *Langmuir*, 2015, **31**, 12783–12796.

7 J. Canivet, A. Fateeva, Y. Guo, B. Coasne and D. Farrusseng, *Chem. Soc. Rev.*, 2014, **43**, 5594–5617.

8 S. K. Henninger, F. P. Schmidt and H.-M. Henning, *Appl. Therm. Eng.*, 2010, **30**, 1692–1702.

9 L. W. Wang, R. Z. Wang and R. G. Oliveira, *Renewable Sustainable Energy Rev.*, 2009, **13**, 518–534.

10 S. R. Batten, N. R. Champness, X.-M. Chen, J. Garcia-Martinez, S. Kitagawa, L. Öhrström, M. O'Keeffe, M. Paik Suh and J. Reedijk, *Pure Appl. Chem.*, 2013, **85**, 1715–1724.

11 W. Lu, Z. Wei, Z.-Y. Gu, T.-F. Liu, J. Park, J. Park, J. Tian, M. Zhang, Q. Zhang, T. Gentle III, M. Bosch and H.-C. Zhou, *Chem. Soc. Rev.*, 2014, **43**, 5561–5593.

12 N. Stock and S. Biswas, *Chem. Rev.*, 2012, **112**, 933–969.

13 J. Ehrenmann, S. K. Henninger and C. Janiak, *Eur. J. Inorg. Chem.*, 2011, **2011**, 471–474.

14 B. B. Saha, I. I. El-Sharkawy, T. Miyazaki, S. Koyama, S. K. Henninger, A. Herbst and C. Janiak, *Energy*, 2015, **79**, 363–370.

15 F. Jeremias, D. Fröhlich, C. Janiak and S. K. Henninger, *RSC Adv.*, 2014, **4**, 24073.

16 D. Fröhlich, S. K. Henninger and C. Janiak, *Dalton Trans.*, 2014, **43**, 15300–15304.

17 D. Fröhlich, E. Pantatosaki, P. D. Kolokathis, K. Markey, H. Reinsch, M. Baumgartner, M. A. van der Veen, D. E. De Vos, N. Stock, G. K. Papadopoulos, S. K. Henninger andC. Janiak, *J. Mater. Chem. A*, 2016, **4**, 11859–11869.

18 J.-P. Zhang, A.-X. Zhu, R.-B. Lin, X.-L. Qi and X.-M. Chen, *Adv. Mater.*, 2011, **23**, 1268–1271.

19 A. Cadiau, J. S. Lee, D. Damasceno Borges, P. Fabry, T. Devic, M. T. Wharmby, C. Martineau, D. Foucher, F. Taulelle, C.-H. Jun, Y. K. Hwang, N. Stock, M. F. De Lange, F. Kapteijn, J. Gascon, G. Maurin, J.-S. Chang and C. Serre, *Adv. Mater.*, 2015, **27**, 4775–4780.

20 F. Jeremias, V. Lozan, S. K. Henninger and C. Janiak, *Dalton Trans.*, 2013, **42**, 15967.

21 M. Kandiah, M. H. Nilsen, S. Usseglio, S. Jakobsen, U. Olsbye, M. Tilset, C. Larabi, E. A. Quadrelli, F. Bonino and K. P. Lillerud, *Chem. Mater.*, 2010, **22**, 6632–6640.

22 M. Kandiah, S. Usseglio, S. Svelle, U. Olsbye, K. P. Lillerud and M. Tilset, *J. Mater. Chem.*, 2010, **20**, 9848.

23 L. Chen, J. Ou, H. Wang, Z. Liu, M. Ye and H. Zou, *ACS Appl. Mater. Interfaces*, 2016, **8**, 20292–20300.

24 A. A. Barkhordarian and C. J. Kepert, *J. Mater. Chem. A*, 2017**, 5**, 5612–5618.

25 Z. Wang, Y. Huang, J. Yang, Y. Li, Q. Zhuang and J. Gu, *Dalton Trans.*, 2017, **46**, 7412–7420.

26 O. Mathon, A. Beteva, J. Borrel, D. Bugnazet, S. Gatla, R. Hino, I. Kantor, T. Mairs, M. Munoz, S. Pasternak, F. Perrin and S. Pascarelli, *J. Synchrotron Radiat.*, 2015, **22**, 1548–1554.

27 N. Stock, *Microporous Mesoporous Mater.*, 2010, **129**, 287–295.

28 A. Coelho, Topas-Academic v5, Brisbane, Australia, 2012.

29 J. H. Cavka, S. Jakobsen, U. Olsbye, N. Guillou, C. Lamberti, S. Bordiga and K. P. Lillerud, *J. Am. Chem. Soc.*, 2008, **130**, 13850–13851.

30 G. C. Shearer, J. G. Vitillo, S. Bordiga, S. Svelle, U. Olsbye and K. P. Lillerud, *Chem. Mater.*, 2016, **28**, 7190–7193.

31 M. Lammert, M. T. Wharmby, S. Smolders, B. Bueken, A. Lieb, K. A. Lomachenko, D. D. Vos and N. Stock, *Chem. Commun.*, 2015, **51**, 12578–12581.

32 W. Liang, C. J. Coghlan, F. Ragon, M. Rubio-Martinez, D. M. D'Alessandro and R. Babarao, *Dalton Trans.*, 2016, **45**, 4496–4500.

33 C. Atzori, G. C. Shearer, L. Maschio, B. Civalleri, F. Bonino, C. Lamberti, S. Svelle, K. P. Lillerud and S. Bordiga, *J. Phys. Chem. C*, 2017, **121**, 9312–9324.

34 L. Valenzano, B. Civalleri, S. Chavan, S. Bordiga, M. H. Nilsen, S. Jakobsen, K. P. Lillerud and C. Lamberti, *Chem. Mater.*, 2011, **23**, 1700–1718.

35 G. C. Shearer, S. Chavan, J. Ethiraj, J. G. Vitillo, S. Svelle, U. Olsbye, C. Lamberti, S. Bordiga and K. P. Lillerud, *Chem. Mater*., 2014, **26**, 4068–4071.

36 S. Øien, D. Wragg, H. Reinsch, S. Svelle, S. Bordiga, C. Lamberti and K. P. Lillerud, *Cryst. Growth Des*., 2014, **14**, 5370–5372.

37 M. J. Cliffe, W. Wan, X. Zou, P. A. Chater, A. K. Kleppe, M. G. Tucker, H. Wilhelm, N. P. Funnell, F.-X. Coudert and A. L. Goodwin, *Nat. Commun*., 2014, **5**, Art. n. 4176.

38 S. Jakobsen, D. Gianolio, D. S. Wragg, M. H. Nilsen, H. Emerich, S. Bordiga, C. Lamberti, U. Olsbye, M. Tilset and K. P. Lillerud, *Phys. Rev. B*, 2012, **86**, Art. n. 125429.

39 W. W. Lestari, P. Lönnecke, H. C. Streit, M. Handke, C. Wickleder and E. Hey-Hawkins, *Eur. J. Inorg. Chem*., 2014, **2014**, 1775–1782.

40 W. W. Lestari, P. Lönnecke, H. C. Streit, F. Schleife, C. Wickleder and E. Hey-Hawkins, *Inorg. Chim. Acta*, 2014, **421**, 392–398.

41 M. Lammert, H. Reinsch, C. A. Murray, M. T. Wharmby, H. Terraschke and N. Stock, *Dalton Trans.*, 2016, **45**, 18822– 18826.

42 J. Sun, D. Zhang, L. Wang, R. Zhang, J. Wang, Y. Zeng, J. Zhan, J. Xu and Y. Fan, *J. Solid State Chem.*, 2013, **206**, 286–292.

43 T. Lee, Y. H. Chang and H. L. Lee, *CrystEngComm*, 2017, **19**, 426–441.

44 A. S. Yasin, J. Li, N. Wu and T. Musho, *Phys. Chem. Chem. Phys*., 2016, **18**, 12748–12754.

45 J. Yang, Y. Dai, X. Zhu, Z. Wang, Y. Li, Q. Zhuang, J. Shi and J. Gu, *J. Mater. Chem. A*, 2015, **3**, 7445–7452.

46 Y. Dong, H. Zhang, F. Lei, M. Liang, X. Qian, P. Shen, H. Xu, Z. Chen, J. Gao and J. Yao, *J. Solid State Chem*., 2017, **245**, 160–163.

47 Y.-A. Li, C.-W. Zhao, N.-X. Zhu, Q.-K. Liu, G.-J. Chen, J.-B. Liu, X.-D. Zhao, J.-P. Ma, S. Zhang and Y.-B. Dong, *Chem. Commun*., 2015, **51**, 17672–17675.

48 D. Yang, V. Bernales, T. Islamoglu, O. K. Farha, J. T. Hupp, C. J. Cramer, L. Gagliardi and B. C. Gates, *J. Am. Chem. Soc*., 2016, **138**, 15189–15196.

49 H. Kummer, M. Baumgartner, P. Hügenell, D. Fröhlich, S. K. Henninger and R. Gläser*, Appl. Therm. Eng*., 2017, **117**, 689–697.